

Quantification of optical pulsed-plane-wave-shaping by chiral sculptured thin films

Joseph B. Geddes III and Akhlesh Lakhtakia

CATMAS—Computational & Theoretical Materials Sciences Group,

Department of Engineering Science & Mechanics,

The Pennsylvania State University,

University Park, PA, 16802–6812, USA

(Received 00 Month 200x; In final form 00 Month 200x)

The durations and average speeds of ultrashort optical pulses transmitted through chiral sculptured thin films (STFs) were calculated using a finite-difference time-domain algorithm. Chiral STFs are a class of nanoengineered materials whose microstructure comprises parallel helicoidal nanowires grown normal to a substrate. The nanowires are $\sim 10\text{--}300$ nm in diameter and $\sim 1\text{--}10$ μm in length. Durations of transmitted pulses tend to increase with decreasing (free-space) wavelength of the carrier plane wave, while average speeds tend to increase with increasing wavelength. An increase in nonlinearity, as manifested by an intensity-dependent refractive index in the frequency domain, tends to increase durations of transmitted pulses and decrease average speeds. The circular Bragg phenomenon exhibited by a chiral STFs manifests itself in the frequency domain as high reflectivity for normally incident carrier plane waves whose circular polarization state is matched to the structural handedness of the film and whose wavelength falls in a range known as the Bragg regime; films of the opposite structural handedness reflect such plane waves little. This effect tends to distort the shapes of transmitted pulses with respect to the incident pulses, and such shaping can cause sharp changes in some measures of average speed with respect to carrier wavelength. A local maximum in the variation of one measure of the pulse duration with respect to wavelength is noted and attributed to the circular Bragg phenomenon. Several of these effects are explained via frequency-domain arguments. The presented results serve as a foundation for future theoretical and experimental studies of optical pulse propagation through causal, nonlinear, nonhomogeneous, and anisotropic materials.

1 Introduction

An ultrashort optical pulse is a pulse of light of duration less than ~ 10 optical periods, where the optical period is calculated from the dominant wavelength in the pulse spectrum. Such ultrashort pulses are generated with commonly implemented mode-locked lasers, and several schemes for compressing and amplifying them have been formulated [1]. Optical pulses are used for micromachining [2], lidar [3, 4], and quantum control and probing of wavepackets and chemical reactions [5, 6]; and their use has been suggested for telecommunications [7].

It is necessary to understand how ultrashort optical pulses propagate in materials in order to design new materials and devices to manipulate them. Earlier, we reported on the spatiotemporal evolution of ultrashort optical pulses as they propagate through complex nano-engineered materials called sculptured thin films (STFs). A STF is a unidirectionally nonhomogeneous, anisotropic medium whose morphology, which consists of an array of parallel shaped nanowires, is engineered by design [8]. The morphology of STFs may break certain translational and rotational symmetries, and these films possess dispersive dielectric and possibly dispersive magnetic properties in the optical regime.

The circular Bragg phenomenon is exhibited by chiral STFs due to their periodic nonhomogeneity and structural chirality arising from the constituent nanowires being nanohelices as shown in the electron micrograph of Figure 1. As circularly polarized monochromatic light propagates through vacuum, the electric field traces out a helix. If the handedness of this helix matches that of the nanohelices in a chiral STF, and if the wavelength of the light lies within a range of wavelengths called the Bragg regime, the light normally incident on the chiral STF is mostly reflected; if the handedness of the helix is opposite, the reflection is little. In the time domain, the circular Bragg phenomenon is manifested as a pulse-bleeding phenomenon [9, 10].

Previous research has shown that chiral STFs can affect the shapes, durations, and energy content of ultrashort optical pulses depending on the circular polarization state of the incident carrier plane

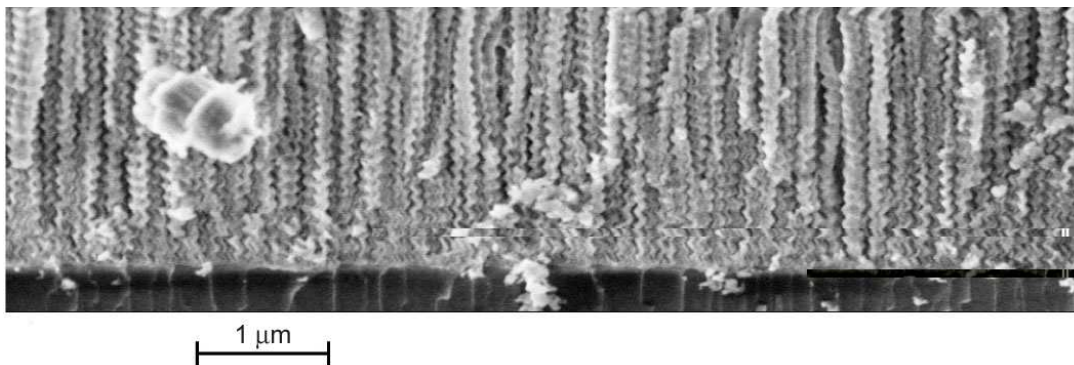


Figure 1. Scanning electron micrograph of a chiral sculptured thin film; note the periodic helical morphology (Courtesy: M. W. Horn, The Pennsylvania State University).

wave [10]. As the thickness of a chiral STF increases, the circular Bragg phenomenon ripens: the reflection first increases and then saturates, and differences in shape and duration between incident and transmitted pulses arise [11]. Ultrawideband pulsed plane waves, known as videopulses, ultranarrowband rectangular pulsed plane waves, and two-dimensional pulsed beams can therefore also be shaped by chiral STFs [12–14]. Pre- and post-resonance Bragg regimes have also been elucidated [15].

So far, all research into the shaping of pulsed plane waves and pulsed beams by chiral STFs has been of a qualitative nature. The shapes of pulses reflected, refracted, transmitted, and diffracted by chiral STFs were predicted numerically, but measures of the extent of pulse shaping were not introduced. Our purpose here is to apply three measures of the pulse duration—the equivalent, root mean square, and correlation durations—and three measures of the average speed of the pulse—the peak speed, the center-of-energy speed, and the correlation speed—to the shaping of pulsed plane waves of different total energies, carrier wavelengths, and carrier polarization states after transmission through linear and nonlinear chiral STFs.

This work is important for four reasons. First, the measures of pulse shaping will allow direct comparisons between our theoretical conclusions and future experiments. Second, quantification of pulse shaping by complex materials like STFs will facilitate the design of STFs to shape pulsed plane waves and pulsed beams in controlled ways. Third, the algorithms we develop can be used to evaluate designs of STF-based devices; and fourth, they advance the state of the art of the time-domain analysis of electromagnetic pulse propagation to include propagation in causal, inhomogeneous, anisotropic, and nonlinear materials.

Parenthetically, by virtue of mathematical isomorphism we expect our results to hold, in general, for cholesteric liquid crystals (CLCs) too. We note that others have modeled optical propagation in noncausal nonlinear cholesteric liquid crystals (CLCs) in the frequency domain [16] and with the slowly-varying envelope approximation [17]; propagation in linear CLCs has also been undertaken with the finite element method [18]. Second harmonic generation in nonlinear chiral STFs was also studied previously in the frequency domain [19]. Our work distinguishes itself from these earlier studies on account of its causal time-domain treatment of the propagation of pulsed plane waves through nonlinear chiral STFs without the invocation of the frequency domain or slowly varying envelope approximation.

Our report on the quantification of the shaping of pulsed plane waves by chiral STFs proceeds as follows. The constitutive relations of a chiral STF, along with a finite-difference scheme for calculating the propagation of pulsed plane waves through vacuum and chiral STFs, are presented in Section 2. Measures of the durations and average speeds of pulsed plane waves are also introduced in Section 2. We discuss the main results of our work in Section 3, and present the main scientific and technological conclusions in Section 4.

2 Theory

This section describes the constitutive relations of spatially local, dielectric, structurally chiral STFs; our choice of ultrashort optical pulses; the numerical method we use to predict their propagation; and three

measures each of pulse duration and speed.

2.1 Maxwell curl postulates and constitutive relations

We begin with the source-free time-domain Maxwell curl postulates

$$\nabla \times \underline{E}(\underline{r}, t) = -\partial_t \underline{B}(\underline{r}, t) , \quad (1)$$

$$\nabla \times \underline{H}(\underline{r}, t) = \partial_t \underline{D}(\underline{r}, t) , \quad (2)$$

where \underline{E} and \underline{B} represent the primitive macroscopic electric and magnetic fields, respectively, while \underline{D} and \underline{H} are the corresponding induction fields. The electromagnetic field is a function of \underline{r} , the position vector, and t , the time. We employ a cartesian coordinate system defined by the set of unit vectors $\{\underline{u}_x, \underline{u}_y, \underline{u}_z\}$. The time derivative is denoted by ∂_t .

A spatially local, dielectric, structurally chiral STF possesses the constitutive relations

$$\underline{D}(\underline{r}, t) = \epsilon_0 \underline{E}(\underline{r}, t) + \underline{P}(\underline{r}, t) , \quad (3)$$

$$\underline{B}(\underline{r}, t) = \mu_0 \underline{H}(\underline{r}, t) , \quad (4)$$

where ϵ_0 is the permittivity and μ_0 is the permeability of vacuum. The polarization \underline{P} is related to the electric field by the following equation:

$$\underline{P}(\underline{r}, t) = \epsilon_0 \int_0^t \underline{\chi}_e(\underline{r}, t') \cdot \left(1 + p_{nl} |\underline{E}(\underline{r}, t - t')|^2\right) \underline{E}(\underline{r}, t - t') dt' . \quad (5)$$

When $p_{nl} = 0$, the film exhibits a linear response to an applied field. When $p_{nl} \neq 0$, the response is third-order nonlinear; specifically, the material exhibits an intensity-dependent refractive index [19, 20]. The nonlinearity is thus isotropic. Whether linear or nonlinear, the chosen material does not respond instantaneously to the applied field.

The dielectric susceptibility dyadic $\underline{\chi}_e(\underline{r}, t)$ contains the information about the nonhomogeneous, anisotropic, and temporally nonlocal properties of a chiral STF. Suppose the chiral STF occupies the region $[z_L, z_R]$. Then the dielectric susceptibility dyadic, which is null-valued in the region $z \notin [z_L, z_R]$, can be factored as:

$$\underline{\chi}_e(\underline{r}, t) = \underline{\underline{S}}(z - z_L) \cdot \underline{\chi}_{ref}(t) \cdot \underline{\underline{S}}^{-1}(z - z_L) , \quad z \in [z_L, z_R] , \quad (6)$$

where $\underline{\underline{S}}$ is a rotation dyadic that describes the morphology of the chiral STF along the z axis (the axis of nonhomogeneity), and $\underline{\chi}_{ref}(t)$ is a reference susceptibility dyadic that describes, in accord with causality, the time-dependent and anisotropic response of the material. In this paper we treat unidirectionally nonhomogeneous STFs, and therefore exclude the recently fabricated bi- and tri- directionally nonhomogeneous films from consideration [21, 22].

The rotation dyadic takes the form

$$\underline{\underline{S}}(z) = \underline{\underline{S}}_z(z) \cdot \underline{\underline{S}}_y(\alpha) , \quad (7)$$

where the dyadic

$$\underline{\underline{S}}_z(z) = \cos\left(\frac{\pi z}{\Omega}\right) (\underline{u}_x \underline{u}_x + \underline{u}_y \underline{u}_y) + h \sin\left(\frac{\pi z}{\Omega}\right) (\underline{u}_y \underline{u}_x - \underline{u}_x \underline{u}_y) + \underline{u}_z \underline{u}_z \quad (8)$$

depends on the structural half period Ω and the structural handedness parameter h , and the dyadic

$$\underline{\underline{S}}_y(\alpha) = \cos \alpha (\underline{u}_x \underline{u}_x + \underline{u}_z \underline{u}_z) + \sin \alpha (\underline{u}_z \underline{u}_x - \underline{u}_x \underline{u}_z) + \underline{u}_y \underline{u}_y \quad (9)$$

depends on the angle of rise α . The chiral STF is either structurally right-handed when $h = 1$ or structurally left-handed when $h = -1$.

The reference susceptibility dyadic, which takes on an orthorhombic form due to the physical vapor deposition process by which chiral STFs are made [8], is defined as

$$\underline{\underline{\chi}}_{ref}(t) = \chi_1(t) \underline{u}_x \underline{u}_x + \chi_2(t) \underline{u}_y \underline{u}_y + \chi_3(t) \underline{u}_z \underline{u}_z, \quad (10)$$

where

$$\chi_\beta(t) = p_\beta \omega_\beta \exp\left(-\frac{\omega_\beta t}{2\pi N_\beta}\right) \sin(\omega_\beta t) \mathcal{U}(t), \quad \beta = 1, 2, 3, \quad (11)$$

is determined both by the oscillator strengths p_β and by the parameters λ_β and N_β , which quantify the resonance wavelengths and absorption characteristics of the film; here, $\omega_\beta = 2\pi c_0/\lambda_\beta$ are the resonance angular frequencies and $\mathcal{U}(t)$ is the unit step function. The Lorentzian dependences (11) are based on a classical material model that treats the charges in a material as undergoing damped oscillations when disturbed from equilibrium by an electric field [23].

2.2 Matrix partial differential equation

We consider pulsed plane waves incident normally on chiral STFs, and hence there is no variation in the electromagnetic field along the x and y directions—i.e., $\partial_x \equiv \partial_y \equiv 0$. Upon writing the components of the electromagnetic field in a 6-vector as $[\underline{F}(z, t)] = [E_x, E_y, E_z, H_x, H_y, H_z]^T$, where the superscript T indicates the transpose, and substituting the constitutive relations into the Maxwell curl postulates (1) and (2), we obtain the matrix partial differential equation

$$\partial_t [\underline{F}(z, t)] = c_0 [\underline{V}] \partial_z [\underline{F}(z, t)] - (1/\epsilon_0) \partial_t [\underline{Q}(z, t)]. \quad (12)$$

In this equation,

$$[\underline{V}] = \begin{bmatrix} 0 & 0 & 0 & 0 & -\eta_0 & 0 \\ 0 & 0 & 0 & \eta_0 & 0 & 0 \\ 0 & 0 & 0 & 0 & 0 & 0 \\ 0 & 1/\eta_0 & 0 & 0 & 0 & 0 \\ -1/\eta_0 & 0 & 0 & 0 & 0 & 0 \\ 0 & 0 & 0 & 0 & 0 & 0 \end{bmatrix} \quad (13)$$

is the vacuum propagation matrix, $\eta_0 = \sqrt{\mu_0/\epsilon_0}$ being the impedance of vacuum and $c_0 = 1/\sqrt{\epsilon_0\mu_0}$ the speed of light in vacuum, and the column vector

$$[\underline{Q}(z, t)] = [P_x(z, t), P_y(z, t), P_z(z, t), 0, 0, 0]^T \quad (14)$$

$$= \epsilon_0 \int_0^t \left(1 + p_{nl} |\underline{E}(z, t - t')|^2\right) [\underline{W}(z, t')] [\underline{F}(z, t - t')] dt'. \quad (15)$$

In the previous equation,

$$[\underline{\underline{W}}(z, t)] = \begin{bmatrix} [\underline{\underline{\chi}}_e(z, t)] & [\underline{\underline{0}}] \\ [\underline{\underline{0}}] & [\underline{\underline{0}}] \end{bmatrix} \quad (16)$$

contains the linear material properties, with $[\underline{\underline{0}}]$ as the 3×3 null matrix. We denote the matrix equivalents of vectors and dyadics by enclosing the corresponding symbols in square brackets.

Equation (12) can only be solved approximately, analytical solutions being virtually impossible for the materials being considered here. It was discretized with respect to both z and t , using the leapfrog method. The details are available elsewhere [24].

2.3 Incident pulsed plane waves

We chose the incident signal as a carrier plane wave that is amplitude-modulated by a pulse envelope $\psi(t)$, i.e., at $z = 0$ we prescribe the boundary condition

$$[\underline{\underline{F}}(0, t)] = \psi(t) \begin{bmatrix} \cos(\omega_{car}t) \\ \cos(\omega_{car}t + \phi) \\ 0 \\ -(1/\eta_0) \cos(\omega_{car}t + \phi) \\ (1/\eta_0) \cos(\omega_{car}t) \\ 0 \end{bmatrix} \mathcal{U}(t), \quad (17)$$

where $\omega_{car} = 2\pi c_0/\lambda_{car}$ is the carrier angular frequency and λ_{car} is the carrier wavelength, while ϕ is a carrier phase. When $\phi = \pi/2$, the carrier plane wave is right circularly polarized (RCP); when $\phi = -\pi/2$, the carrier plane wave is left circularly polarized (LCP). The initial condition was chosen to be $[\underline{\underline{F}}(z, 0)] = [\underline{\underline{0}}]$.

Even though we treat pulsed plane waves in this paper, it should be noted that no electromagnetic signal—or STF—can have an infinite transverse extent; indeed, all physical electromagnetic signals are pulsed beams. However, the pulsed-plane-wave approximation to a pulsed beam is appropriate when the beamwidth is much larger than the carrier wavelength (but still smaller than the transverse extent of the STF). The characteristics of two-dimensional pulsed beam propagation in chiral STFs have been reported elsewhere [14].

We chose the pulse envelope $\psi(t)$ to be gaussian, so that

$$\psi(t) = \sqrt{\frac{\eta_0 U_t}{\tau_0 \sqrt{\pi}}} \exp\left(-\frac{1}{2} \left(\frac{t - t_d}{\tau_0}\right)^2\right), \quad t > 0, \quad (18)$$

but $\psi(t) = 0$ for $t \leq 0$. The time constant τ_0 governs the duration of the pulse, while t_d is the time delay which permits the whole pulsed plane wave to enter the computation domain. The prefactor on the right side of (18) is chosen so that

$$\int_{-\infty}^{\infty} S_z(z, t) dt = U_t, \quad (19)$$

$S_z = \underline{u}_z \cdot (\underline{E} \times \underline{H})$ being the axial component of the instantaneous Poynting vector. Hence, U_t is the total energy per unit area of the incident pulsed plane wave.

2.4 Quantification of pulse durations and average speeds

We now turn to quantitative measures of pulse duration and average speed. Our goal is to define measures that are useful for experimental research or theoretical insight or both. As the chosen pulses are highly broadband and suffer appreciable distortion, the usual concept of group velocity [25] is not meaningful for analysis except in frequency-domain arguments. More sophisticated measures were therefore devised.

The pulse duration is an important parameter because it determines the time scale for measurements or manipulations made with the pulse; pulses of shorter duration permit the measurement of events of shorter duration [26]. In order to define measures of pulse duration, we considered the m^{th} moment $\mathcal{M}_{f,\xi}^{(m)}$ of a scalar function $f(\xi)$ with respect to variable ξ on the interval $[\xi_a, \xi_b]$:

$$\mathcal{M}_{f,\xi}^{(m)}(f(\xi), [\xi_a, \xi_b]) = \int_{\xi_a}^{\xi_b} \xi^m f(\xi) d\xi. \quad (20)$$

The root mean square (RMS) deviation $\sigma_{f,\xi}$ from the centroid

$$\zeta_{f,\xi}(f(\xi), [\xi_a, \xi_b]) = \frac{\mathcal{M}_{f,\xi}^{(1)}(f(\xi), [\xi_a, \xi_b])}{\mathcal{M}_{f,\xi}^{(0)}(f(\xi), [\xi_a, \xi_b])} \quad (21)$$

of $f(\xi)$ with respect to ξ on the interval $[\xi_a, \xi_b]$ is defined as follows [27]:

$$\sigma_{f,\xi}(f(\xi), [\xi_a, \xi_b]) = \sqrt{\frac{1}{\mathcal{M}_{f,\xi}^{(0)}(f(\xi), [\xi_a, \xi_b])} \int_{\xi_a}^{\xi_b} (\xi - \zeta_{f,\xi})^2 f(\xi) d\xi}, \quad (22)$$

$$= \sqrt{\frac{\mathcal{M}_{f,\xi}^{(2)}(f(\xi), [\xi_a, \xi_b])}{\mathcal{M}_{f,\xi}^{(0)}(f(\xi), [\xi_a, \xi_b])} - \zeta_{f,\xi}^2(f(\xi), [\xi_a, \xi_b])}. \quad (23)$$

Both $\zeta_{f,\xi}$ and $\sigma_{f,\xi}$ are undefined when $\mathcal{M}_{f,\xi}^{(0)}(f(\xi), [\xi_a, \xi_b]) = 0$.

One measure of the pulse duration, as evaluated over a time interval $[t_a, t_b]$ at a point z_r , is

$$\tau_u = 2\sigma_{U,t}(U(z_r, t), [t_a, t_b]), \quad (24)$$

where the electromagnetic energy density

$$U(z, t) = \epsilon_0 |\underline{E}(z, t)|^2 + \mu_0 |\underline{H}(z, t)|^2. \quad (25)$$

Alternatively, we could compute the RMS deviations from the centroid of $S_z(z, t)$ or the intensity $|\underline{E}(z, t)|^2$ with respect to time. Another measure of the pulse duration, called the equivalent duration [27], is $\mathcal{M}_{U,t}^{(0)}$ computed at a particular z_r over an interval $[t_a, t_b]$, and divided by the peak value of $U(z_r, t)$ over that interval, i.e.,

$$\tau_p = \frac{\mathcal{M}_{U,t}^{(0)}(U(z_r, t), [t_a, t_b])}{\text{Max}(U(z_r, t), [t_a, t_b])}, \quad (26)$$

where Max indicates the maximum value of a function over the chosen time interval. The correlation duration τ_c is defined by [27]

$$\tau_c = \frac{\int_{-\infty}^{\infty} \int_{-\infty}^{\infty} U(z_r, t) U(z_r, t + t') dt' dt}{\mathcal{M}_{U^2,t}^{(0)}(U^2(z_r, t), (-\infty, \infty))}. \quad (27)$$

We decided to use τ_p , τ_u , and τ_c as measures of pulse duration in this study.

There are many measures of the pulse speed, including the group speed and the centrovelocity [28]. We calculated three measures of the speed of the pulse through the film: the average speed of the pulse's peak value of $U(z_r, t)$, the average speed of $\zeta_{U,t}$, and the average correlation velocity [29]. The energy density $U(z_r, t)$ of the transmitted pulse was recorded over the interval $[t_a, t_b]$ at some location $z_r > z_R$. Then the time

$$t_p = t_{\text{Max}}(U(z_r, t), [t_a, t_b]) \quad (28)$$

where the function t_{Max} indicates the time at which the maximum value of its argument occurs, the time

$$t_u = \zeta_{U,t}(U(z_r, t), [t_a, t_b]), \quad (29)$$

and the time

$$t_c = t_d + t_{\text{Max}}\left(\int_0^\infty U(0, t') U(z_r, t + t') dt'\right) \quad (30)$$

were found. From these data, the average speeds c_p , c_u , and c_c were calculated from the formula

$$\frac{c_\beta}{c_0} = \frac{z_R - z_L}{c_0(t_\beta - t_d) - (z_r - (z_R - z_L))}, \quad \beta = p, u, c. \quad (31)$$

Thus the speeds c_p , c_u , and c_c are the thickness of the chiral STF divided by the computed times t_p , t_u , and t_c , less the time over which the pulse traverses the vacuous regions $0 < z < z_L$ and $z_R < z < z_r$. We note that these measures are average speeds because they are in the form of a finite distance over a finite time interval, and hence do not reveal variations in the speed of the pulse as it enters, traverses, and exits the chiral STF. For the foregoing calculations, we approximated integrals with the rectangular rule [30].

The measures of pulse duration and average speed have different physical meanings and concomitant advantages and disadvantages. The equivalent duration τ_p is the duration a rectangular pulse would have, if it possessed the same peak value of $U(z_r, t)$ and the same total energy per unit area as the pulse under consideration. Its advantage lies with its simplicity; however, it depends crucially on the correct determination of the peak value of $U(z_r, t)$. This same problem is a disadvantage of c_p , which is the average speed of the peak of the pulse through the chiral STF. This measure of the speed can even become multi-valued if the peak value of $U(z_r, t)$ occurs at more than one local maximum (like the twin humps of a Bactrian camel).

The duration τ_u is the RMS deviation of $U(z_r, t)$ from its first moment, normalized to the total energy per unit area of the pulse. It is analogous to the concept of radius of gyration in mechanics. We call c_u , the average speed of $\zeta_{U,t}$, the center-of-energy speed. It is analogous to the concept of the velocity of a body's center of mass in mechanics, and is closely related to the centrovelocity and a redefinition of the group velocity¹, as discussed elsewhere [28]. The advantage of these measures is that they depend on $U(z_r, t)$ over the whole pulse, and not just on the peak value of $U(z_r, t)$. However, it is possible for the center of energy to be located at a value of z at which $U(z, t) = 0$ [29].

The correlation duration τ_c is a measure of how tightly $U(z_r, t)$ is concentrated in time. The correlation velocity c_c is the average speed of the peak of the correlation of the incident pulse with the transmitted pulse. Like c_p , it depends heavily on the shape of the transmitted pulse. In some cases, it could become a multi-valued function of z_r and the chosen time interval $[t_a, t_b]$. However, it does provide a way to track the propagation of energy in the pulse in a different way than c_u , and it is fairly robust [29].

All six of the quantities we have defined in this subsection are amenable to experimental determination, for example by frequency-resolved optical gating (FROG) [26]. In our definitions of the measures, we

¹The centrovelocity is the velocity of $\zeta_{|E|^2,t}(|E|^2(z_r, t), [t_a, t_b])$ [28].

have chosen to use $U(z_r, t)$ instead of $|\underline{E}(z_r, t)|^2$, for example, because the former is a Lorentz-invariant quantity.

3 Results and discussion

We now turn to a discussion of the results of our calculations.

3.1 Constitutive and excitation parameters

The chiral STF we studied possesses the following constitutive parameters: $p_1 = 0.52$, $p_2 = 0.42$, $p_3 = 0.40$, $N_{1,2,3} = 100$, $\lambda_1 = 290$ nm, $\lambda_{2,3} = 280$ nm, $\Omega = 200$ nm, and $\alpha = 20^\circ$. The film is structurally right-handed, i.e., $h = +1$, and we chose it to be either linear (i.e., $p_{nl} = 0$) or nonlinear ($p_{nl} = 3 \times 10^{-24}$ m²/V²), in accord with simple order-of-magnitude estimates [31]. We fixed $z_L = 30$ μ m and $z_R = 34$ μ m; thus, the chiral STF is ten pitches thick. The variable z was discretized into intervals of $\Delta z = 2$ nm, and the variable t into intervals of $\Delta t = 6.34 \times 10^{-3}$ fs. The center wavelength of the Bragg regime of the linear chiral STF is approximately 516 nm, and its full-width half-maximum bandwidth is approximately 27 nm [10, 32], though we note that both these quantities may change slightly when the chiral STF is nonlinear [33]. For all the results presented here, the incident pulse has the time constant $\tau_0 = 2$ fs and time delay $t_d = 8$ fs. We calculated for three different combinations of material nonlinearity and incident pulse energy per unit area:

- Case L: a linear film, with $U_t = 1 \times 10^6$ J/m²,
- Case N1: a nonlinear film, with $U_t = 1 \times 10^6$ J/m², or
- Case N2: a nonlinear film, with $U_t = 2 \times 10^6$ J/m².

Two indexes of refraction that govern the speed of monochromatic plane waves through a linear chiral STF are [8] $n_2(\lambda_0) = \sqrt{\hat{\epsilon}_2(\lambda_0)}$ and $n_d(\lambda_0) = \sqrt{\hat{\epsilon}_d(\lambda_0)}$ where

$$\hat{\epsilon}_\ell(\lambda_0) = 1 + \hat{\chi}_\ell(\lambda_0) = 1 + \frac{p_\ell \omega_\ell \left[\omega_\ell^2 \left[1 + (2\pi N_\ell)^{-2} \right] - \left(\frac{2\pi c_0}{\lambda_0} \right)^2 + i \left(\frac{2c_0 \omega_\ell}{N_\ell \lambda_0} \right) \right]}{\left[\omega_\ell^2 \left[1 + (2\pi N_\ell)^{-2} \right] - \left(\frac{2\pi c_0}{\lambda_0} \right)^2 \right]^2 + \left(\frac{2c_0 \omega_\ell}{N_\ell \lambda_0} \right)^2}, \quad \ell = 1, 2, 3, \quad (32)$$

and

$$\hat{\epsilon}_d(\lambda_0) = \frac{\hat{\epsilon}_1(\lambda_0) \hat{\epsilon}_3(\lambda_0)}{\hat{\epsilon}_1(\lambda_0) \sin^2 \alpha + \hat{\epsilon}_3(\lambda_0) \cos^2 \alpha}, \quad (33)$$

where $\hat{\cdot}$ indicates the temporal Fourier transform and λ_0 is the free-space wavelength. Plots of the real and imaginary parts of $n_2(\lambda_0)$ and $n_d(\lambda_0)$ are shown in Figure 2. The corresponding phase velocities

$$v_{p2} = c_0 / \text{Re}(n_2), \quad (34)$$

$$v_{pd} = c_0 / \text{Re}(n_d), \quad (35)$$

and group velocities

$$v_{g2} = c_0 / \text{Re}(n_2 + \omega \partial_\omega n_2), \quad (36)$$

$$v_{gd} = c_0 / \text{Re}(n_d + \omega \partial_\omega n_d), \quad (37)$$

are shown in Figure 3; here, $\omega = 2\pi c_0 / \lambda_0$ and $\partial_\omega \equiv \partial / \partial \omega$. These frequency-domain plots help to explain our time-domain results.

3.2 Reflected and transmitted pulses

The spatiotemporal evolution of the incoming pulse was computed on the spatial domain $z \in [0, 60] \mu\text{m}$, of which the chiral STF occupies $z \in [30, 34] \mu\text{m}$. Measures of pulse duration and speed were computed at $z_r = 36 \mu\text{m}$ over the time interval $[0, 190] \text{ fs}$. The wavelength λ_{car} of the carrier plane wave was set to either 415, 515, or 615 nm; and the polarization state of the carrier plane wave was chosen as either LCP or RCP. At visible wavelengths, the selected linear constitutive properties yield refractive indexes that are commonplace in optics [34].

Let us now examine the effects of the chiral STFs on pulses reflected from and transmitted through them. We are interested mainly in trends in the pulse shape, duration, and speed as the pulse energy per unit area, carrier wavelength and polarization state, and the nonlinearity of the chiral STF are varied, as opposed to particular values that the duration, etc., may take on as those parameters are varied. The shapes of the incident pulses, as exemplified by snapshots of their energy density in Figure 4, are independent both of the carrier wavelength and carrier polarization state. The incident pulses traversed vacuum ($z \in [0, 30] \mu\text{m}$), were scattered by the STF, and eventually became transmitted signals in the vacuous region $z \in [34, 60] \mu\text{m}$ and reflected signals in the region $z \in [0, 30] \mu\text{m}$.

Let us begin with Case L. Both transmitted and reflected pulses are captured in the snapshots of $U(z, t)$ at time $t = 190 \text{ fs}$ in Figure 5, where an important trend can be perceived. Irrespective of the polarization state of the carrier plane wave, the peak energy density of the transmitted pulse increases with increasing carrier wavelength. That is, the peak value of $U(z, t)$, $z > z_R$, is greater when $\lambda_{car} = 615 \text{ nm}$ than when $\lambda_{car} = 515$ or 415 nm for a given carrier polarization state. This trend applies in reverse to the lengths (i.e., z -extents) of the transmitted pulses: the transmitted pulses are longer when λ_{car} takes on lower values.

The effects of structural handedness are most evident in the plots of the reflected pulses shown in Figure 6, which contains plots of $U(z, t)$ as a function of time at $z = 27.6 \mu\text{m}$. The incident pulse is either LCP or RCP, and $\lambda_{car} = 415, 515$, or 615 nm . The energy densities of the reflected pulses (which begin at $t \approx 110 \text{ fs}$) are much smaller than those of the incident pulses.

The effects of the circular Bragg phenomenon are evident in Figure 6. In the bottom row of plots, for which the conditions for the circular Bragg phenomenon are satisfied [10], the primary reflected pulse possesses both a larger head and longer tail *than* when the incident carrier plane wave is LCP (top row of plots). The longer tail is due to the bleeding of energy from the refracted pulse inside the film to the reflected pulse [10], and it is most pronounced when $\lambda_{car} = 515 \text{ nm}$, i.e. when the carrier wavelength lies in the Bragg regime.

A secondary pulse appears in all six cases beginning at $t \approx 155 \text{ fs}$. This smaller pulse is the result of the reflection from the chiral STF / vacuum interface at $z = z_R$. When the incident light is RCP, $U(z, t)$ at $z < z_L$ oscillates rapidly in both the head of the primary pulse and the secondary pulse, a phenomenon that is due to interference between LCP and RCP components of the reflected light [33]. The tail of the primary reflected pulse does not exhibit such large oscillations because a superposition of LCP and RCP light of substantially the same energy densities is needed to create them [33]. The LCP component of the reflected pulse is of short duration, on the order of the duration of the incident pulse. The pulse-bleeding effect only operates on the fraction of incident light in the Bragg regime that is RCP, and so the tail of the primary reflected pulse contains mostly RCP light but little to no LCP light when the circular Bragg phenomenon occurs.

Corresponding plots for the nonlinear Cases N1 and N2 are shown in Figures 7 and 8, respectively. While still small compared to the incident pulses', the peak values of $U(z, t)$ in the heads of the primary reflected pulses increase from Figures 6 to 8 for given carrier wavelength and polarization state. This is due to the increasing effects of nonlinearity in Case N1 as compared to Case L, and in Case N2 as compared to Case N1. An understanding emerges from the frequency domain [10, 15, 33] as follows: for the type of nonlinearity we studied, a greater value of U_t creates a greater refractive-index mismatch between vacuum and the chiral STF because of the multiplicative character of the nonlinearity in (5) [33]. The refractive index of vacuum is unity, and we can see from Figure 2 that the real parts of $n_2 \neq 1$ and $n_d \neq 1$ are decreasing functions of carrier wavelength at carrier wavelengths greater than 300 nm. When the chiral STF is nonlinear, the differences between the refractive indexes of the chiral STF and unity shall become even greater, and those differences will be greatest when the intensity of the beam is highest. Hence, the

reflection at the pulse head is greater than otherwise.

The peak values of $U(z, t)$ in the secondary pulses are not appreciably different from Case L to Case N1 to Case N2 (at least when normalized by the value of U_t , as was done for all the figures). Evidently, absorption by the chiral STF reduces the peak energy density of the primary refracted pulse in Case N2 to a greater degree than in Case N1 and in Case N1 to a greater degree than in Case L [33]. In the frequency domain, absorption manifests itself through positive values of $\text{Im}(n_2)$ and $\text{Im}(n_d)$, as seen in Figure 2. By the time the primary refracted pulses reach z_R , their energy densities drop such that the refractive-index mismatch between vacuum and chiral STF across $z = z_R$ is reduced between Cases L, N1, and N2. Differences in energy density that remained were further reduced on the return trip of the secondary pulse from $z = z_R$ to $z = z_L$.

Figures 9 to 11 contain plots of $U(z, t)$ as functions of time recorded at $z = 36 \mu\text{m}$; these are the transmitted pulses for Cases L, N1, and N2, respectively. The peak values of $U(z, t)$ increase, for given carrier polarization state, as λ_{car} increases, an effect that is attributable to the presence of the absorption resonances at ultraviolet wavelengths. The frequency domain behavior of the absorption resonances is shown in plots of $\text{Im}(n_2)$ and $\text{Im}(n_d)$ in Figure 2. Other parameters being equal, more of the bandwidth of a pulse with lower λ_{car} overlaps the bandwidth of the absorption resonances of the chiral STF than the bandwidth of a pulse with higher λ_{car} , and hence more absorption occurs in the former case. For given λ_{car} and carrier polarization state, the peak values of $U(z, t)$ —again normalized to U_t —drop from Figures 9 to 11. Notice that when the incident carrier plane wave is RCP, but not LCP, the transmitted pulses tend to have a lobed or humped structure, and that the number and sizes of the lobes increase from Case L to Case N1 to Case N2. Thus, the presence of the chosen nonlinearity distorts the shapes of the transmitted pulses and tends to make them highly asymmetric, but the effect is prominent only when the structural handedness of the film matches the sense of the circular polarization state of the incident carrier plane wave.

3.3 Durations of transmitted pulses

What effects does a change in carrier wavelength have on the durations of pulses transmitted through a chiral STF? Quantification of the effects of the carrier wavelength, carrier polarization state, and the nonlinearity of the chiral STF on τ_p , τ_u , and τ_c is provided through Figure 12, wherein plots of those quantities for thirteen values of λ_{car} ranging from 395 to 635 nm are shown. The incident carrier plane wave is again either LCP or RCP, and Cases L, N1, and N2 are again considered. The overall trend in the plots is a decrease in pulse duration with increasing carrier wavelength. As the carrier wavelength decreases, the material exhibits greater dispersion due to proximity to the absorption resonances. The transmitted pulse is consequently of longer duration, because light of longer free-space wavelength has both greater phase and group velocities in the chiral STF than light of shorter λ_0 , as can be seen in Figure 3. This is because $n_2(\lambda_0)$ and $n_d(\lambda_0)$ drop with increasing λ_0 above the resonance wavelengths $\lambda_{1,2,3}$, as can be seen in Figure 2. Therefore the chosen pulses, which do not possess any negative chirp in their carrier wavelengths, tend to spread out as they propagate through the chiral STF.

Although that is the overall trend, there is an exception: there appears to be a local maximum for τ_u when $\lambda_{car} \approx 515 \text{ nm}$ and the incident carrier plane wave is RCP. We believe that this effect is due to the circular Bragg phenomenon, because the local maximum appears in the vicinity of the center wavelength of the Bragg regime, and it does not appear when the incident carrier plane wave is LCP. Additionally, for the same λ_{car} and carrier polarization state, the duration of the pulses tends to increase from Case L to Case N1 to Case N2.

3.4 Average transmission speed through chiral STF

Plots of c_p , c_u , and c_c in Figure 13 show that they all tend to increase with increasing carrier wavelength, but decrease slightly with increasing nonlinearity. These two trends are due to the presence of the absorption resonances in the ultraviolet regime, and the tendency of the nonlinearities to enhance those resonances. As is clear from Figure 2, the principal refractive indexes of the chiral STF are higher for wavelengths

closer to the resonances, and hence pulsed plane waves with lower λ_{car} are slowed more by the film than pulsed plane waves with higher λ_{car} , as can be seen in Figure 3.

The presence of nonlinearity increases the refractive indexes because of its multiplicative nature in (5), and hence pulsed plane waves with higher U_t are slowed more than pulsed plane waves with lower U_t when propagating through a chiral STF. Both c_p and c_c are heavily affected by pulse shaping by the chiral STF which is manifested as the alteration of the peaks of the transmitted pulses. For example, notice the jumps in these quantities that occur between $\lambda_{car} = 455$ nm and $\lambda_{car} = 475$ nm for Cases N1 and N2 when the incident carrier plane wave is RCP. The jumps occur due to the appearance of the lobed structure of the transmitted pulses mentioned in Section 3.2; and, in the case of c_c , also due to the short duration of the incident pulse as compared to the transmitted one. The calculations of c_p and c_c require finding the peak value of either $U(z_r, t)$ or of its correlation with the $U(0, t)$; and so, if one lobe suddenly becomes larger than another, the peak of the transmitted pulse has to shift. This shift creates a jump in both c_p and c_c . Pulse shaping is to be expected to be particularly prominent when pulses of high peak powers pass through nonlinear chiral STFs, because the effects of nonlinearity are going to be very pronounced then.

4 Concluding remarks

As a result of our calculations, we offer the following conclusions that may be useful to future designers of optical pulse shapers fabricated with chiral STFs.

- Increased nonlinearity reshapes pulses more—as is evident in the increased formation of a lobed structure—when the carrier polarization state of the incident pulse has the same sense as the structural handedness of the chiral STF. Attenuation of the transmitted pulse increases when the carrier wavelength lies closer to the absorption resonances, which is also confirmed by frequency-domain results [15, 32].
- For specified carrier polarization state, U_t , and p_{nl} , the durations τ_p , τ_u , and τ_c all tend to increase with decreasing λ_{car} —except for τ_u in the case of a linear chiral STF under conditions in which the circular Bragg phenomenon is exhibited. Therefore a chiral-STF-based device could change the durations of pulses, contingent on the polarization state of the incident carrier plane wave.
- For specified λ_{car} and polarization state of the incident carrier plane wave, the transmitted pulse duration tends to increase with increasing nonlinear effects. Therefore, any pulse-shaping device based on nonlinear chiral STFs can only be expected to work over a certain range of incident pulse intensities.
- For a given carrier polarization state, U_t , and p_{nl} , the speed c_u tends to increase with increasing λ_{car} . Therefore chiral STFs can function as wavelength-selective delay elements for ultrashort optical pulses.
- For specified λ_{car} and polarization state of the incident carrier plane wave, the speeds c_p , c_u , and c_c tend to decrease with increasing nonlinear effects.

To conclude, let us note that our presented technique can accommodate other types of nonlinearities—specifically, nonlinearities that are not simply multiplicative but must be incorporated through multiple convolutions, which appear necessary for modelling the nonlinear response of dielectrics to attosecond pulses [20]. However, the computational capabilities then required will be significantly greater than the ones commonly available today.

Acknowledgments: We thank the Pittsburgh Supercomputing Center for computer resources used to develop the computer programs used in this work. Joseph B. Geddes III thanks both the National Science Foundation (NSF) for an NSF Graduate Research Fellowship and SPIE for a SPIE Educational Scholarship. We are grateful for the reviews of two anonymous referees and an editor whose comments helped us improve the presentation of our work.

References

- [1] GOSNELL, T. R., and TAYLOR, A. J. (Editors), 1991, *Selected Papers on Ultrafast Laser Technology* (Bellingham, WA, USA: SPIE Press).

- [2] LIU, X., DU, D., and MOUROU, G., 1997, *IEEE J. Quantum Electron.*, **33**, 1706.
- [3] RAIROUX, P., SCHILLINGER, H., NIEDERMEIER, S., et al., 2000, *Appl. Phys. B*, **71**, 573.
- [4] RODRIGUEZ, M., BOURAYOU, R., MÉJEAN, G., et al., 2004, *Phys. Rev. E*, **69**, 036607-1.
- [5] KOHLER, B., YAKOVLEV, V. V., CHE, J., et al., 1995, *Phys. Rev. Lett.*, **74**, 3360.
- [6] ZEWAHL, A. H., 1993, *J. Phys. Chem.*, **97**, 12427.
- [7] KNOX, W. H., 2000, *IEEE J. Sel. Top. Quantum Electron.*, **6**, 1273.
- [8] LAKHTAKIA, A., and MESSIER, R., 2005, *Sculptured Thin Films: Nanoengineered Morphology and Optics* (Bellingham, WA, USA: SPIE Press).
- [9] GEDDES III, J. B., MEREDITH, M. W., and LAKHTAKIA, A., 2000, *Opt. Commun.*, **182**, 45.
- [10] GEDDES III, J. B., and LAKHTAKIA, A., 2001, *Eur. Phys. J. Appl. Phys.*, **13**, 3. Erratum: 2001, **16**, 247.
- [11] GEDDES III, J. B., and LAKHTAKIA, A., 2001, *Eur. Phys. J. Appl. Phys.*, **14**, 97. Erratum: 2001, **16**, 247.
- [12] GEDDES III, J. B., and LAKHTAKIA, A., 2002, *Eur. Phys. J. Appl. Phys.*, **17**, 21.
- [13] GEDDES III, J. B., and LAKHTAKIA, A., 2001, *Microwave Opt. Technol. Lett.*, **28**, 59.
- [14] GEDDES III, J. B., and LAKHTAKIA, A., 2005, *Opt. Commun.*, **252**, 307.
- [15] WANG, J., LAKHTAKIA, A., and GEDDES III, J. B., 2002, *Optik*, **113**, 213.
- [16] FU, P., YE, P., YU, Z., et al., 1987, *J. Opt. Soc. Am. B*, **4**, 1392.
- [17] AVENDAÑO, C. G., and REYES, J. A., 2004, *Phys. Rev. E*, **70**, 061701-1.
- [18] HONG, Q., WU, T. X., and WU, S.-T., 2003, *Liq. Cryst.*, **30**, 367.
- [19] VENUGOPAL, V. C., and LAKHTAKIA, A., 1998, *Proc. Roy. Soc. Lond. A*, **454**, 1535.
- [20] HELLWARTH, R. W., 1977, *J. Prog. Quant. Electr.*, **5**, 1.
- [21] HORN, M. W., PICKETT, M. D., MESSIER, R., et al., 2004, *Nanotechnology*, **15**, 303.
- [22] HORN, M. W., PICKETT, M. D., MESSIER, R., et al., 2004, *J. Vac. Sci. Technol. B*, **22**, 3426.
- [23] BOHREN, C. F., and HUFFMAN, D. R., 1983, *Absorption and Scattering of Light by Small Particles* (New York, NY, USA: John Wiley & Sons).
- [24] GEDDES III, J. B., 2006, *Manipulation of Optical Pulses with Chiral Sculptured Thin Films*, PhD Thesis (University Park, PA, USA: The Pennsylvania State University).
- [25] OUGHSTUN, K. E., and SHERMAN, G. C., 1994, *Electromagnetic Pulse Propagation in Causal Dielectrics* (Berlin, Germany: Springer-Verlag).
- [26] TREBINO, R., 2000, *Frequency-Resolved Optical Gating: The Measurement of Ultrashort Laser Pulses* (Boston, MA, USA: Kluwer).
- [27] BRACEWELL, R. N., 2000, *The Fourier Transform and Its Applications*, 3rd Edition (New York, NY, USA: McGraw Hill).
- [28] SMITH, R. L., 1970, *Am. J. Phys.*, **38**, 978.
- [29] BLOCH, S. C., 1977, *Am. J. Phys.*, **45**, 538.
- [30] JALURIA, Y., 1996, *Computer Methods for Engineering* (Washington, DC, USA: Taylor & Francis).
- [31] BOYD, R. W., 1999, *J. Mod. Opt.*, **46**, 367.
- [32] LAKHTAKIA, A., 1999, *Eur. Phys. J. Appl. Phys.*, **8**, 129.
- [33] GEDDES III, J. B., and LAKHTAKIA, A., 2003, *Opt. Commun.*, **225**, 141.
- [34] MACLEOD, H. A., 2001, *Thin-Film Optical Filters*, 3rd Edition (Philadelphia, PA, USA: Institute of Physics Publishing).

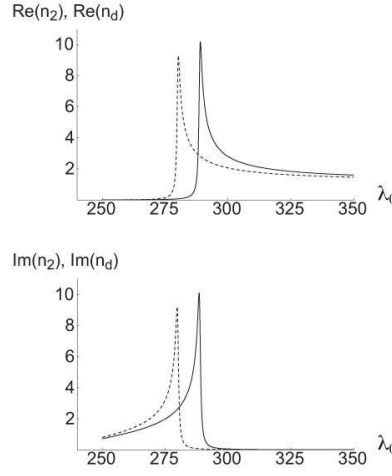


Figure 2. Plots of $\text{Re}(n_2)$ (top, dashed), $\text{Re}(n_d)$ (top, solid), $\text{Im}(n_2)$ (bottom, dashed), and $\text{Im}(n_d)$ (bottom, solid) as functions of free-space wavelength λ_0 (in nm). Note that these quantities decrease with increasing λ_0 for $\lambda_0 > 300$ nm.

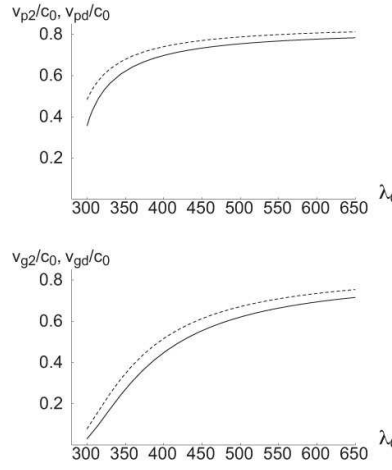


Figure 3. Plots of v_{p2}/c_0 (top, dashed), v_{pd}/c_0 (top, solid), v_{g2}/c_0 (bottom, dashed), and v_{gd}/c_0 (bottom, solid) as function of free-space wavelength λ_0 (in nm). Note that these quantities increase with increasing λ_0 .

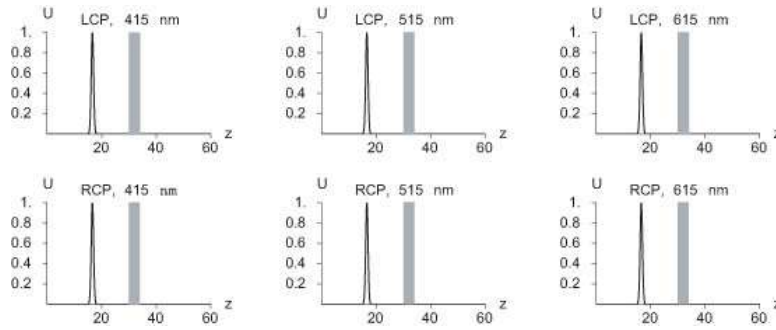


Figure 4. Plots of $U(z, t)$ (in arbitrary units) of the incident pulses as a function of z (in μm) for $\lambda_{car} = 415$ nm (left), 515 nm (center), and 615 nm (right) recorded at time $t = 63.4$ fs. The incident carrier plane wave is either LCP (top) or RCP (bottom); note that the plots are identical regardless of carrier wavelength or polarization. The chiral STF, indicated by the shaded area, occupies the region $z \in [30, 34]$ μm . The values of $U(z, t)$ have been multiplied by a factor of $c_0\tau_0\sqrt{\pi}/U_t$; hence, the shapes of the incident pulses in these plots are independent of U_t also.

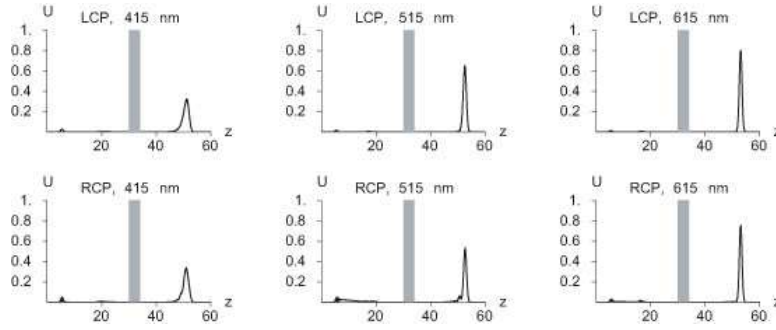


Figure 5. Same as Figure 4, except that the data are recorded at time $t = 190$ fs, and so reflected (left of film) and transmitted (right of film) pulses are captured. The chiral STF is structurally right-handed and linear (Case L).

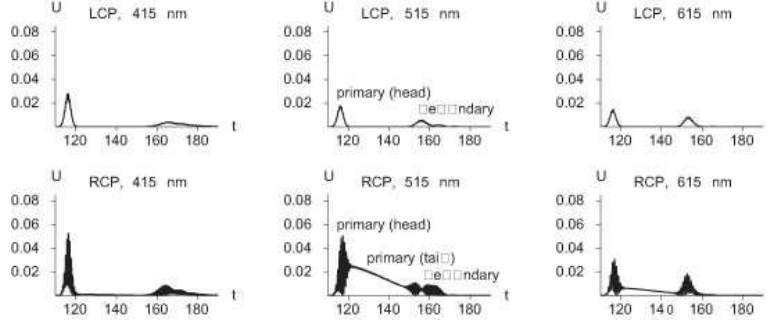


Figure 6. Plots of $U(z, t)$ (in arbitrary units) as a function of time t (in fs) for $\lambda_{car} = 415$ nm (left), 515 nm (center), and 615 nm (right) recorded at $z = 27.6 \mu\text{m}$. The incident carrier plane wave is either LCP (top) or RCP (bottom). The primary and secondary reflected pulses are captured in the record. The chiral STF is structurally right-handed and linear (Case L). The values of $U(z, t)$ are multiplied by a factor of $c_0\tau_0\sqrt{\pi}/U_t$, where $U_t = 1 \times 10^6 \text{ J/m}^2$.

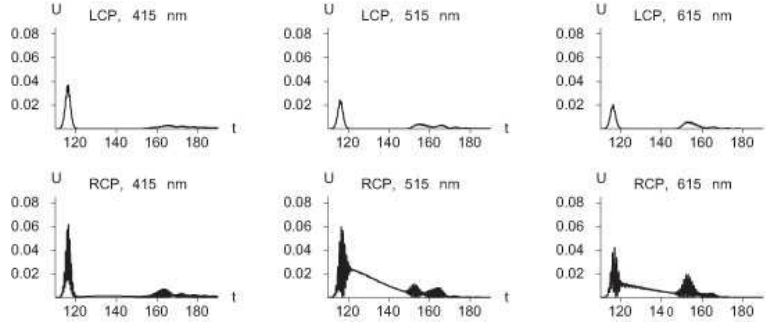


Figure 7. Same as Figure 6, except that the chiral STF is nonlinear (Case N1).

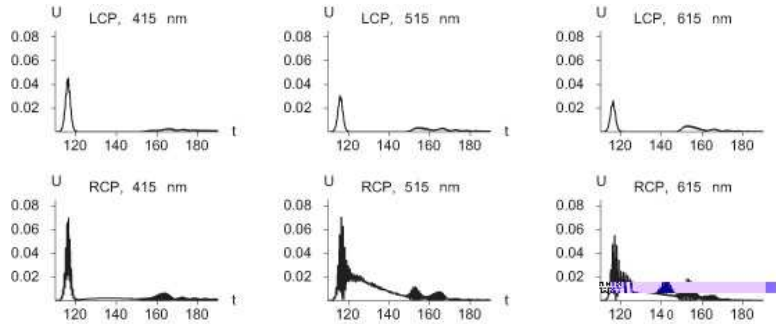


Figure 8. Same as Figure 7, except that $U_t = 2 \times 10^6 \text{ J/m}^2$ (Case N2).

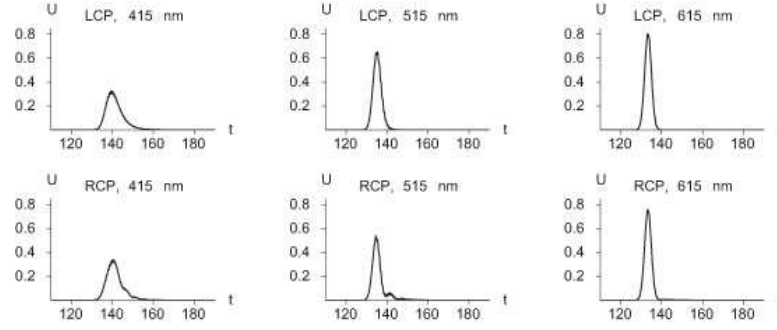


Figure 9. Plots of $U(z, t)$ (in arbitrary units) as a function of time t (in fs) for $\lambda_{car} = 415$ nm (left), 515 nm (center), and 615 nm (right) recorded at $z = 36 \mu\text{m}$, and so the transmitted pulses are captured in the record. The incident carrier plane wave is either LCP (top) or RCP (bottom), and the chiral STF is structurally right-handed and linear (Case L). The values of $U(z, t)$ are multiplied by a factor of $c_0\tau_0\sqrt{\pi}/U_t$, where $U_t = 1 \times 10^6 \text{ J/m}^2$.

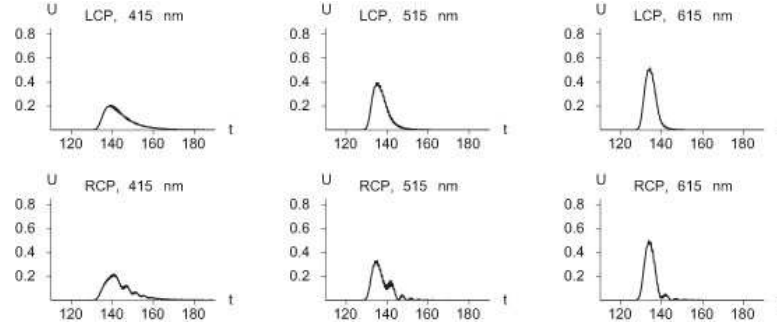


Figure 10. Same as Figure 9, except that the chiral STF is nonlinear (Case N1).

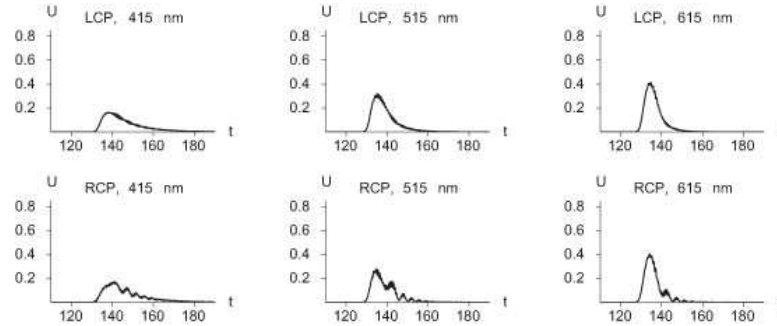


Figure 11. Same as Figure 10, except that $U_t = 2 \times 10^6 \text{ J/m}^2$ (Case N2).

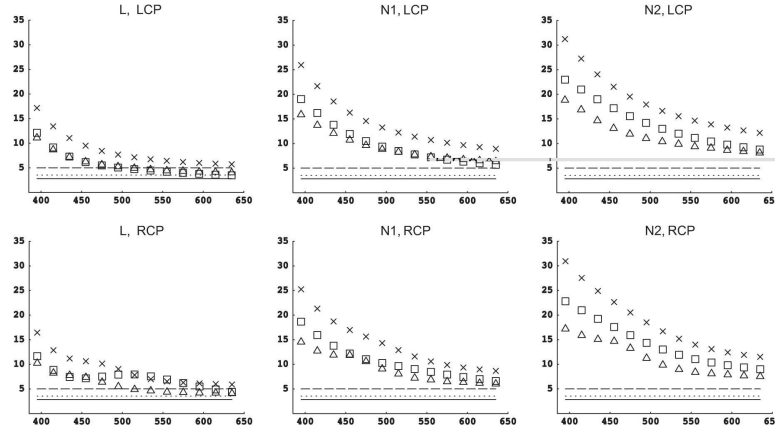


Figure 12. Durations τ_p (Δ , in fs), τ_u (\square , in fs), τ_c (\times , in fs) as functions of carrier wavelength λ_{car} (in nm) for six different cases, evaluated at $z_r = 36 \mu\text{m}$ over the interval $[0, 190]$ fs. The incident carrier plane wave is either LCP (top) or RCP (bottom). In addition, the chiral STF is either linear ($p_{nl} = 0$) while $U_t = 1 \times 10^6 \text{ J/m}^2$ (Case L, at left); nonlinear ($p_{nl} = 3 \times 10^{-24} \text{ m}^2/\text{V}^2$) while $U_t = 1 \times 10^6 \text{ J/m}^2$ (Case N1, in center); or nonlinear ($p_{nl} = 3 \times 10^{-24} \text{ m}^2/\text{V}^2$) while $U_t = 2 \times 10^6 \text{ J/m}^2$ (Case N2, at right). The lines at the bottom of each plot indicate the value of τ_p (dotted), τ_u (solid), and τ_c (dashed) for the incident pulses.

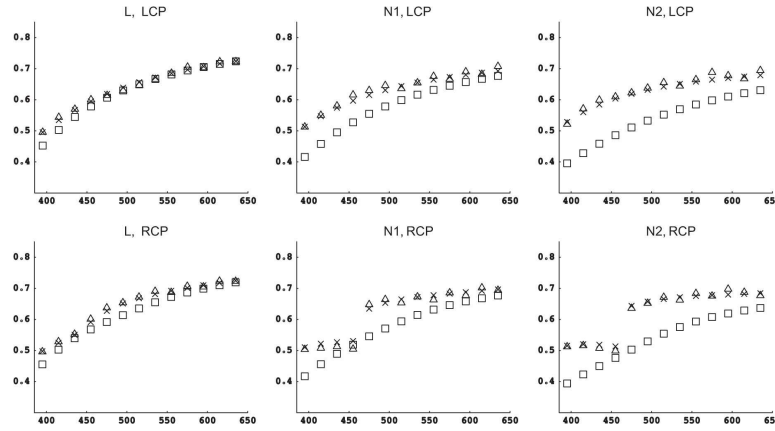


Figure 13. Normalized average speeds c_p/c_0 (Δ), c_u/c_0 (\square), and c_c/c_0 (\times) as functions of carrier wavelength λ_{car} (in nm) for six different cases, evaluated at $z_r = 36 \mu\text{m}$ over the interval $[0, 190]$ fs. The incident carrier plane wave is either LCP (top) or RCP (bottom). In addition, the chiral STF is either linear ($p_{nl} = 0$) while $U_t = 1 \times 10^6 \text{ J/m}^2$ (Case L, at left); nonlinear ($p_{nl} = 3 \times 10^{-24} \text{ m}^2/\text{V}^2$) while $U_t = 1 \times 10^6 \text{ J/m}^2$ (Case N1, in center); or nonlinear ($p_{nl} = 3 \times 10^{-24} \text{ m}^2/\text{V}^2$) while $U_t = 2 \times 10^6 \text{ J/m}^2$ (Case N2, at right).